Chemical Engineering Journal 348 (2018) 978–991

Contents lists available at ScienceDirect

Chemical Engineering Journal

journal homepage: www.elsevier.com/locate/cej

Macroscopic fuel reactor modelling of a 5 kW_{th} interconnected fluidized bed for in-situ gasification chemical looping combustion of coal

Hongpeng Xu, Jinchen Ma, Haibo Zhao*

State Key Laboratory of Coal Combustion, School of Energy and Power Engineering, Huazhong University of Science and Technology, Wuhan 430074, PR China

HIGHLIGHTS

- A model is developed for the combustion of coal in a novel 5 kw fluidized bed system.
- The fluid dynamics and mass transfer in the fuel reactor with a riser are simulated.
- The model predicts the effects of different operation conditions on the performance.
- The sensitivity analysis for the efficiency of combustion and carbon capture is done.

ARTICLE INFO

Keywords:
Macroscopic model
Chemical-looping combustion
CO_2 capture
Simulation
Sensitivity analysis

ABSTRACT

A macroscopic model is developed to simulate the fluid dynamics with the transfer of heat and mass in the fuel reactor and the riser of a novel 5 kW_{th} interconnected fluidized bed system for chemical looping combustion of coal. The fuel reactor and the riser are divided into a bottom bed consisting of bubble and emulsion phases, a freeboard with splash and transport phases, a transition zone with different cross-section areas and a riser providing the driving force to recirculate solids between the fuel and air reactors. The developed model is validated by the experimental cases with different operation conditions such as thermal power, temperature and coal feeding rate. Subsequently, the effects of reactor temperature, solids inventory, oxygen carrier to coal ratio and compositions of the fluidizing agent on the reactor performance are analyzed in details by the help of the validated model. The sensitivity analysis shows that the reactor temperature is the most relevant parameter affecting the combustion efficiency and CO_2 capture efficiency. Furthermore, increasing the oxygen carrier to coal ratio increases the combustion efficiency but decreases the CO_2 capture efficiency, while increasing the volume fraction of CO_2 in the fluidizing agent has the opposite effect on the performance of this experimental unit.

1. Introduction

Chemical looping combustion (CLC) technology has been considered as a very promising CO_2 capture technology from fossil fuel combustion [1,2]. The oxygen carrier transfers the oxidizer from the air reactor to the fuel reactor, so that the fuel no longer mix with the air directly in the fuel reactor. Since gas emissions mainly consist of CO_2 and H_2O, the nearly pure CO_2 can be captured with less energy consumption in comparison with the conventional CO_2 capture technologies.

The plenty of oxygen carriers are required as the bed material to supply the oxidizer and to be heat carrier circulating between the fuel reactor and the air reactor. The interconnected fluidized bed reactor system has been the most popular reactor for CLC, because this reactor configuration can intensify the contact between gas and particles and circulate the bed inventory between two reactors. Lyngfelt et al. proposed the design criterion of an interconnected fluidized bed reactor system for CLC [3] and operated a continuous 10 kW_{th} CLC reactor using gaseous fuel [4]. Their works demonstrated the feasibility of this reactor for the CLC technology. Designing and using different interconnected fluidized bed reactor systems, several research groups successfully applied CLC to solid fuels [5–14]. The performance of these reactors, such as fuel conversion, the distribution of carbonaceous gases, the residence time of solid materials, are mainly determined by the behavior in the fuel reactor [15,16]. The operation conditions of the fuel reactor also have great influence on the risk of agglomeration/sintring and attrition/fragmentation that impair the reactivity of oxygen carriers and pose a negative effect on the fuel conversion

* Corresponding author.
E-mail address: hzhao@mail.hust.edu.cn (H. Zhao).

https://doi.org/10.1016/j.cej.2018.05.025
Received 13 January 2018; Received in revised form 3 May 2018; Accepted 5 May 2018
Available online 07 May 2018
1385-8947/

Nomenclature

A_0	gas distributor area per nozzle
A_c	section area of the fuel reactor (m^2)
Ar	Archimedes number
C_{bottom}	solid concentration in the bottom bed
$C_{freeboard}$	solid concentration in the freeboard bed
$C_{c\text{-}a}$	solid concentration in the core-annulus zone
C_{spl}	solid concentration in the splash phase
C_{tran}	solid concentration in the transition zone
C_{carbon}	carbon concentration in the fuel
$C_{b,i}$	concentration of gas compositions in bubble phase
$C_{e,i}$	concentration of gas compositions in emulsion phase
$C_{g,i}$	concentration of gas for reduction of oxygen carriers
D_B	diameter of bubbles (m)
d_i	stoichiometric coefficient for gas combustion
d_p	diameter of bed material (m)
E	activation energy
F_b	flow of gas compositions in the bubble phase (mol/s)
F_{char}	flow of carbon exiting from the fuel reactor (mol/s)
F_{coal}	rate of coal feeding (kg/s)
F_e	flow of gas compositions in the emulsion phase (mol/s)
F_{exc}	flow of gas from the emulsion to bubble phase(mol/s)
F_d	drag force
F_{dil}	flow of gas compositions in the dilute phase (mol/s)
F_p	friction between particles and wall
F_{OC}	solid circulation rate (kg/s)
F_w	friction between gas and wall
$F_{w,j}$	solid flow by the wall-layer (kg/s)
F_{WGS}	flow of gas composition from WGS reaction (mol/s)
H_{bot}	height of bottom bed zone (m)
H_r	height of reactor (m)
k_{be}	coefficient of mass transfer between emulsion and bubble phase
k_g	mass transfer coefficient
K	chemical parameters for the reaction rate
Mw	molecular mass (kg/kmol)
P	pressure (Pa or Bar)
r_g	grain radius (μm)
R	mass transfer resulted from chemical reaction (kg/m^3 s)
R_{OC}	oxygen transport capacity of the oxygen carriers
S_{area}	section area (m^2)
t_r	mean reaction time (s)
t_{mr}	mean residence time (s)
u_g	gas velocity (m/s)
U_g	superficial gas velocity (m/s)
U_{mf}	minimal fluidization velocity (m/s)
U_B	velocity of bubble phase (m/s)
$U_{g,int}$	velocity of interstitial gas velocity (m/s)
U_t	terminal velocity of particles (m/s)
u_g	real velocity of gas (m/s)
V	volume of each cell (m^3)
x	mass fraction
X	mass fraction
X_{OC}	conversion rate of oxygen carriers
$\overline{X_{OC}}$	mean conversion rate of oxygen carriers
$\overline{X_{OC,in}}$	mean conversion rate of oxygen carriers at the inlet of the fuel reactor
$\overline{X_{OC,out}}$	mean conversion rate of oxygen carriers at the outlet of the fuel reactor
X_{char}	char conversion rate
y_i	molar fraction of gas i

Greek symbols

δ_B	volume fraction of bubble phase
ρ_s	average density of solids (kg/m^3)
$\rho_{m,i}$	molar density of the reacting material (mol/m^3)
ε_s	volume fraction of solids in each cell
ε_g	volume fraction of gas in each cell
ε_B	average bed porosity
τ_i	time for complete solid conversion for the reaction
Ω_{OD}	oxygen demand
η_{comb}	combustion efficiency
η_{CC}	CO_2 capture efficiency

Subscript

mf	minimum fluidization condition
sta	saturation condition
OC	oxygen carrier
int	interstitial gas
WGS	water gas shift reaction

[17,18]. Therefore, it is significant to seek optimized reactor design and operation conditions for the fuel reactor.

Along with the experimental research, the computational fluid dynamics (CFD) [19–21] and the macroscopic model [22–24] provide other essential tools to investigate the fluid dynamics and chemical kinetics in the fuel reactor. Using CFD model, Mahalatkar et al. not only predicted the emission of the fuel reactor but also captured the reasonable conversion rate of solid fuels and oxygen carriers at different reactor temperatures [25]. Emden et al. used the two-fluid model to research the influence of different reactor configuration and operation including buffer position, solid circulation rate and air reactor length on the reduction degree of oxygen carrier in the fuel reactor [20]. Parker carried out the three-dimensional simulation by using the computational particles instead of the real oxygen carrier particles in the circulating fluidized bed [26]. The simulated solid circulation rate and efficiency had good agreement with the experimental measurements.

However, the computational cost of CFD methods is rather high on account of the large amount and the long reaction time of oxygen carriers, especially for the parametric study [24–26]. The macroscopic model maintaining the effect of fluid dynamics based on empirical/semi-empirical expressions, by contrast, can make out the relationship between operation parameters and performance at much lower cost [27]. Pallares and Johnsson reviewed the utilization of macroscopic model in the large-scale circulating fluidized bed [27]. This literature showed that the macroscopic model provided satisfying results of fluid dynamics like the axial volume fraction along the bed, particle size segregation and superficial solids net flow with much lower computation time. Considering the chemical reaction model of oxygen carriers derived from experiments [28], Abad et al. developed a macroscopic model to simulate the CLC of gaseous fuel and solid fuel in the fuel reactor separately [15,29,30]. This developed model was also used to investigate the influence of different parameters on the performance of $1MW_{th}$ chemical-looping combustion of coal, and the optimal temperature and solid inventory were suggested for attaining the maximum carbon separation efficiency [31]. Focusing on developing the model for fuel reactor, Peltola et al. modeled the methane combustion in the dual fluidized bed system and provided a nice method to improve the performance of an pre-commercial scale CLC system [23,32]. Furthermore, the macroscopic model of fuel reactor was used to study the chemical looping with oxygen uncoupling process [33] and the biomass combustion [24].

It has been validated that macroscopic model of the fuel reactor is

very efficient for the design and performance optimization of a new CLC reactor. A new 5 kW_{th} interconnected fluidized bed reactor using coal as fuel has been designed by our research group [34]. The riser installed at the top of the fuel reactor mainly provides the driving force to re-circulate the oxygen carrier in this unit. In order to optimize the reactor performance efficiently, it is important to understand the basic relations between the relevant design and operating parameters based on the macroscopic model. To the best of our knowledge, no model considered both the fluid dynamics and chemical reactions in the fuel reactor and the riser is available in the literature. Therefore, a macroscopic model of fuel reactor is developed by coupling different models of fluid dynamics and chemical reactions in the riser in this work. This developed model is validated by the experimental data. Moreover, the effects of different operation conditions, such as temperature, solid inventory, ratio of different fluidizing gas and oxygen demand on the performance parameters, are analyzed for the optimal operation and the future scale-up consideration.

2. Description of 5 KW_{th} reactor

The modeled reactor is obtained from a 5 kW_{th} interconnected fluidized bed for in-situ gasification chemical looping combustion designed and operated at Huazhong University of Science and Technology in China [34]. Fig. 1 shows the schematic of this experimental unit where arrows represent the flow direction of gas and particles. The fuel reactor system and the air rector system have the similar structure including a reactor, a riser, a cyclone and a loop-seal. The risers are equipped to drive the circulation of bed inventory. The fresh hematite particles are loaded in the fuel reactor, the air reactor and two loop-seals before starting-up the experimental system. The fluidization gas for the air reactor is air, while the bed material in the fuel reactor is fluidized by the mixture of N_2 and CO_2. The electric heater and insulation fixed on the wall are used to maintain the high temperature in two reactors. The coal gasification and pyrolysis products react with oxygen carriers in the fuel reactor. The flue gases of the air reactor and the fuel reactor are measured by the gas analyzer. The performance of this experimental rig is primarily dependent on the combustion process in the fuel reactor system. Therefore, the modelling is focusing on the fluid dynamics and conversion of solids in the fuel reactor and the riser.

3. Methodology

The riser installed at the top of the fuel reactor provides the driving force, which leads to the high-velocity fluidization regime in the upper of the fuel reactor. At the moment, the riser features the fast fluidization. Based on the theory of fluidization and the experimental observation, the flow regime in the fuel reactor is divided into the bubble fluidization and the core-annulus flow structure [27,35]. The fast fluidization in the riser is modeled by solving a set of governing equations. Moreover, the models of chemical reactions are coupled into these governing equations. In this work, the model developed is implemented in Aspen Customer Modeler (ACM) platform [36] which is a simulation environment developed by Aspen Technologies. Based on the positions of the inlet of fluidization gas, the inlet of coal feeding and the inlet of oxygen carriers from the loop seal, and the geometry of the transition zone and the riser, Fig. 2 shows the structure divisions for the fuel reactor and the riser. The governing equations for each division are described in the following part.

3.1. Model of the fuel reactor

The bubbling fluidization regime in the bottom bed is divided into two parts [35]: the bubble phase is assumed to be absence of particles, the emulsion phase consists of solids and gas with the minimum fluidizing velocity. Actually, some interstitial gas can pass through the bubbles and have a velocity defined as $U_{g,int}$. Therefore, the superficial gas velocity in the bottom zone is expressed as:

$$U_g = (1-\delta_B)U_{mf} + U_B + U_{g,int} \quad (1)$$

where the U_g means the superficial gas velocity, δ_B means the volume fraction of bubbles, U_B is the velocity of bubble phase.

The upper zone is characterized by the splash phase and the core-annulus flow. The splash phase begins from the roof of the bottom zone, and considers the back–mixing behavior of solids between the upper zone and the bottom bed. In the core-annulus flow, the solids flow upward in the core and downward in the annulus along the wall of the reactor. The mass transfer of solids between the core and the annulus is also taken into consideration. Therefore, the fluid dynamics in the upper zone is described by the change of solids concentration along the reactor height as:

$$\frac{dC_{spl}}{dz} = -4\frac{U_t}{U_g}C_{spl} \quad (2)$$

$$\frac{dC_{c-a,i}}{dz} = -\frac{0.23}{U_g - U_{t,i}}C_{c-a,i} \quad (3)$$

where the C_{spl} and $C_{c\text{-}a}$ mean the solids concentration in splash phase and the core-annulus flow.

The fundamental behaviors in different zones of the fuel reactor are described above. Abad et al. formulated the model for the fluid dynamics in the fuel reactor in details [15], and the equations used in this work are shown in Table A1.

3.2. Fluid dynamics model in the transition zone and riser

In the transition zone, its length is considerably short, and the velocities of gas and solids are very high. In addition, the mass exchange is neglected because of the fairly short length and residence time of gas and solids. Thus, the conservation equations for up-flow flux through the transition zone are expressed as:

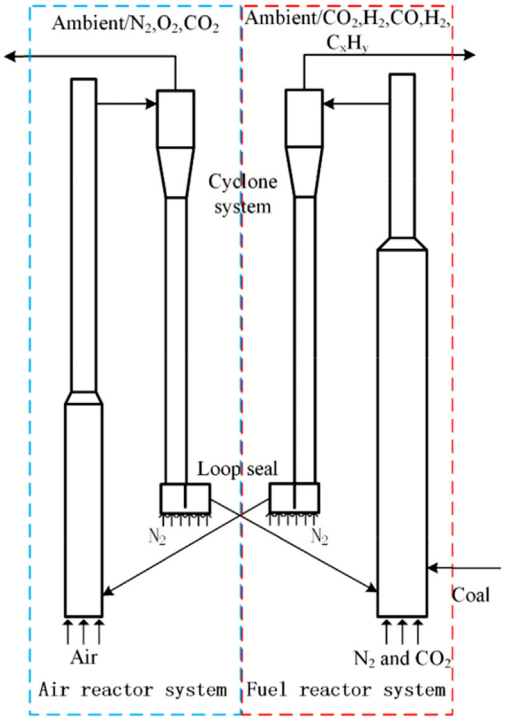

Fig. 1. Schematic of the 5 kW_{th} interconnected fluidized bed for in-situ gasification chemical looping combustion of coal.

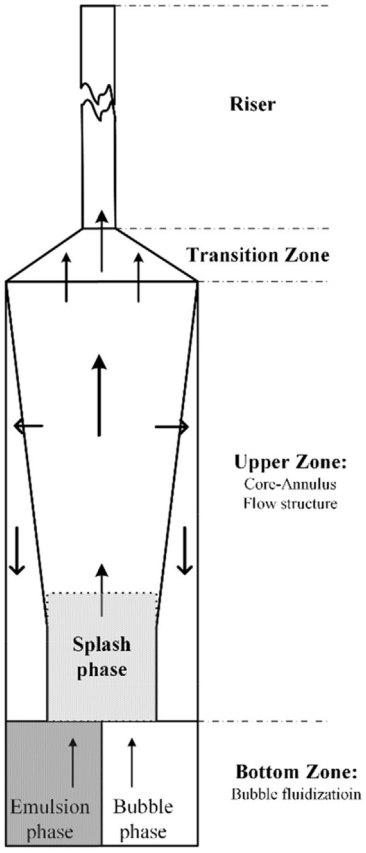

Fig. 2. The schematic of zone division for the fuel reactor and the riser.

$$\frac{d(U_g \rho_g S_{area})}{dx} = 0 \tag{4}$$

$$\frac{d(u_s C_{tran,i} S_{area})}{dx} = 0 \tag{5}$$

It is considered that the pressure drop is resulted from combined effects of the change of solids concentration like in the fuel reactor and the ideal negative throat nozzle.

$$\frac{dP_{transition}}{dz} = \int_0^{H_{tran}} C_{tran} g dz - \frac{d(\rho U_g^2)}{dz} \tag{6}$$

The pneumatic conveying of the riser is always described by the following governing equations [37,38]. The continuity equations for gas and solid phases are:

$$\frac{d(\rho_g u_g \varepsilon_g)}{dz} = \sum_i R_{g,i} \tag{7}$$

$$\frac{d(\rho_s u_s \varepsilon_s)}{dz} = \sum_i R_{s,i} \tag{8}$$

The momentum governing equation for gas-solids mixture is modeled as [37]:

$$\rho_s \varepsilon_s u_s \frac{du_s}{dz} + \rho_g \varepsilon_g u_g \frac{du_g}{dz} = -\frac{dP_{riser}}{dz} + (\varepsilon_s \rho_s + \varepsilon_g \rho_g) g + F_w + F_P \tag{9}$$

where the four terms on the right-hand side represent the pressure drop, the gravitational forces, the gas-wall friction and the particle–wall friction. In order to solve momentum equation, the pressure drop resulted from the two-phase flow is expressed as:

$$\varepsilon_s \frac{dP_{riser}}{dz} = -\rho_s \varepsilon_s \frac{du_s}{dz} + \varepsilon_s \rho_s g + F_d + F_P \tag{10}$$

where F_d is the drag force. Its expression for spherical particles is:

$$F_d = 0.75 C_d \frac{(u_g - u_s)^2}{d_p} \rho_g \varepsilon^{-2.65} \tag{11}$$

where the drag coefficient C_d is expressed as:

$$C_d = \frac{24}{Re_p}(1 + 0.1806 Re_p^{0.6459}) + \frac{0.4251}{1 + \frac{6880.95}{Re_p}} \tag{12}$$

The friction between gas and wall, F_w, is calculated as follows:

$$F_w = \left(0.0056 + \frac{0.5}{Re^{0.32}}\right) \frac{\rho_g \varepsilon_g u_g^2}{2 d_p} \tag{13}$$

The friction between particles and wall, F_p, is expressed as [39]:

$$F_p = 0.0126 \frac{\varepsilon_s}{\varepsilon_g^3} \left(\frac{\varepsilon_s u_t}{u_g - u_s}\right)^{-0.979} \frac{\rho_s \varepsilon_s u_s^2}{2 d_p} \tag{14}$$

3.3. Reactive kinetic model

3.3.1. Coal Pyrolysis and gasification

Table 1 shows the ultimate and proximate analysis of a Chinese bituminous coal as the fuel. It is assumed that the drying and pyrolysis occur instantaneously [15]. The stoichiometric coefficients for the products are determined from coal mass balance [40] and given by:

$$\text{Coal} + 0.0148\ CO_2 \rightarrow 0.79\ \text{Char} + 0.092\ CO + 0.033\ CH_4 + 0.118\ H_2 + 0.021\ H_2O + 0.011\ NH_3 + 0.0027\ H_2S + 0.067\ \text{Ash} \tag{R1}$$

A certain amount of CO_2 is used as the fluidization gas and the gasification agent. The gasification reactions of char with CO_2 and H_2O are as follows:

$$\text{Char} + CO_2 \rightarrow 2\ CO \tag{R2}$$

$$\text{Char} + H_2O \rightarrow CO + H_2 \tag{R3}$$

Based on the shrinking core model, the gasification rates of char with CO_2 and H_2O are calculated as:

$$\dot{m}_{char,CO_2} = \rho_s \varepsilon_s x_{char} \frac{S_0}{1 - \varepsilon_{0,p}} (1 - X_{Char})^{2/3} \frac{k_{CO_2} P_{CO_2}}{1 + K_{CO_2} P_{CO_2} + K_{CO} P_{CO}} \tag{15}$$

$$\dot{m}_{char,H_2O} = \rho_s \varepsilon_s x_{char} \frac{S_0}{1 - \varepsilon_{0,p}} (1 - X_{Char})^{2/3} \frac{k_{H_2O} P_{H_2O}}{1 + K_{H_2O} P_{H_2O} + K_{H_2} P_{H_2}} \tag{16}$$

where the S_0 and $\varepsilon_{0,p}$ represent the initial surface area and porosity of the particles [25]. Table 2 shows the kinetic parameters. The gasification rates vary with the type of coal and temperature [41],so these parameters are tuned for the char used in this work based on the literature [42]. The char particle consists of ash and fixed carbon [15]. The local carbon concentration in the char, $x_{char,}$ is calculated in the

Table 1
Properties of coal and hematite particles.

Proximate analysis (wt%)	Moisture	1.66
	Volatile	15.54
	Ash	34.34
	Fixed Carbon	48.46
Ultimate analysis (wt%)	Carbon	55.26
	Hydrogen	2.12
	Nitrogen	0.79
	Sulfur	0.44
	Oxygen	5.39
Lower heating value	24.8	MJ/kg
Average diameter of Hematite	180	μm
Apparent density of Hematite	3472	kg/m3

Table 2
Kinetic parameters for gasification and water gas shift reaction.

	Pre-exponential factor	Activation energy
k_{CO_2}	$6.0\cdot10^{-7}$ (1/s)	110 (kJ/mol)
K_{CO_2}	$1.37\cdot10^{-5}$ (1/Pa)	16 (kJ/mol)
K_{CO}	$2.1\cdot10^{-5}$ (1/Pa)	–
k_{H_2O}	$5.2\cdot10^{-3}$ (1/s)	221 (kJ/mol)
K_{H_2O}	$9.21\cdot10^{-4}$ (1/Pa)	72 (kJ/mol)
K_{H_2}	4.07 (1/Pa)	–
K_{WGS}	$2.17\cdot10^{7}$	192.9 (kJ/mol)
Keq	exp(4577.8/T − 4.33)	

emulsion phase, splash zone and core-annulus zone as [15]:

$$x_{char} = \left(\frac{C_{j,char}}{C_{j,char} + C_{i,OC}}\right)\left(\frac{(1-X_{char})C_{0,char}}{(1-X_{char})C_{0,char} + C_{0,ash}}\right) \quad (17)$$

3.3.2. Reduction of oxygen carrier particles

The oxygen carrier is hematite with low cost and moderate reactivity [43,44]. The reductions of oxygen carriers are shown as:

$$CH_4 + 12\,Fe_2O_3 \rightarrow 8\,Fe_3O_4 + CO_2 + 2\,H_2O \quad (R4)$$

$$CO + 3\,Fe_2O_3 \rightarrow 2\,Fe_3O_4 + CO_2 \quad (R5)$$

$$H_2 + 3\,Fe_2O_3 \rightarrow 2\,Fe_3O_4 + H_2O \quad (R6)$$

The conversion rate of oxygen carrier particles is modeled by the shrinking core model (SCM) [28,45]:

$$\frac{t}{\tau_i} = 1-(1-X_{OC,i})^{\frac{1}{3}}, \quad \frac{1}{\tau_i} = \frac{b_i k_{oc,i} C_{g,i}^n}{\rho_M r_g} \quad (18)$$

The kinetic constant $k_{oc,i}$ is expressed as the Arrhenius formula:

$$k_{oc,i} = k_{0,oc}\exp(-E_{oc,i}/R_g T) \quad (19)$$

The kinetic parameters for Eq. (18) are shown in Table 3 [45]. The reduction rates of hematite particles are calculated from the average reaction rates of hematite particles [28,29]. The average rates for reaction R4, R5 and R6 at each height cell are expressed as [28]:

$$R_{oc,i} = d_i R_{g,i} = \rho_{m,OC}\frac{\overline{dX_{oc,i}}}{dt} \quad (20)$$

The average conversion rate of hematite particles is calculated as a function of the residence time [28]:

$$\frac{\overline{dX_{OC,i}}}{dt} = \int_0^{t_r} \frac{dX_{OC,i}}{dt}\frac{e^{-t/t_{mr}}}{t_{mr}}dt \quad (21)$$

where t_{mr} represents the mean residence time of hematite particles and is related to the solids recirculation rate and solids inventory. The mean reaction time t_r means how long an hematite particle is reduced from its initial state entering the fuel reactor to the possible maximum variation, and is calculated as [29]:

$$t_{r,i} = \tau_i(1-\overline{X_{OC,in}}) \quad (22)$$

where $\overline{X_{OC,in}}$ is the mean conversion of the hematite particles entering the fuel reactor.

The instantaneous conversion rate in Eq. (21), $X_{OC,i}(t)$, is related to the mean conversion rate at the fuel reactor inlet and the reaction time [15]:

$$X_{OC,i}(t)-\overline{X_{OC,in}} = 1-\left(1-\frac{t}{t_{mr}}\right)^3 \quad (23)$$

The mean conversion of the hematite particles at the fuel reactor outlet, $\overline{X_{OC,out}}$, can be obtained by integral of the instantaneous conversion as:

$$(1-\overline{X_{OC,out}}) = \int_0^{t_{mr}} (1-X_{OC}(t))\frac{e^{-t/t_{mr}}}{t_{mr}}dt \quad (24)$$

According to the iteration of Eqs. (23) and (24), the mean reacting time, $t_{r,m}$, and $\overline{X_{OC,out}}$ can be obtained. The calculated value of $\overline{X_{OC,out}}$ should also fit the relation as:

$$F_{OC}R_{OC}(\overline{X_{OC,out}}-\overline{X_{OC,in}}) = Mw_O[\left(F_{H_2O} + 2F_{CO_2} + F_{CO}\right)_{outlet} - \left(F_{H_2O} + 2F_{CO_2} + F_{CO}\right)_{inlet}] \quad (25)$$

The reduction of oxygen carriers is also concerned with the gas concentration in the Eq. (18). Based on the experimental measurements, Abad et al. suggested that the local gas concentrations are assumed to equal to that on the particle surface, i.e., $C_{g,i} = C_{pg,i}$ [15]. Taking diffusion of the gas compositions through the gas film into account, the value of $C_{pg,i}$ is determined by the following mass balance to a particle:

$$\frac{\rho_s R_{OC}}{b_i M_O}\frac{\pi d_p^3}{6}\frac{d(X_{OC}(t)-\overline{X_{oc,in}})}{dt} = k_{g,i}\pi d_p^2(C_{gz,i}-C_{pg,i}) \quad (26)$$

where $C_{gz,i}$ represents the gas concentration in the bulk gas flow, $k_{g,i}$ is the meaning of mass transfer coefficient. In the bottom zone [46] and upper zone [47], this coefficient is calculated as, separately:

$$k_{g,i}|_{bottom} = (2\varepsilon_z + 0.117Ar^{0.39}Sc^{1/3})D_{g,i}/d_p \quad (27)$$

$$k_{g,i}|_{freeboard} = (2\varepsilon_z + 0.69\mathrm{Re}_p^{0.5}Sc^{1/3})D_{g,i}/d_p \quad (28)$$

3.3.3. Water-gas shift reaction

As the Fe-based material could promote the water–gas shift reaction (WGSR) [31], the WGSR is considered in this work.

$$CO + H_2O \rightarrow CO_2 + H_2 \quad (R7)$$

The reaction rate is calculated as [48]:

$$R_{WGS} = k_{WGS}e^{-E_1/RT}(C_{CO}^{n_1}C_{H_2O}^{n_2} - C_{CO_2}^{n_3}C_{H_2}^{n_4}/K_{eq}) \quad (29)$$

The kinetic parameters for this reactions rate are shown in Table 3.

3.4. Simulation procedure

Some initial conditions are needed to carry out the simulation. Firstly, the pressure drop is directly related to the bed height in the fuel reactor and expressed as:

$$\frac{dP}{dz} = \int_0^{H_{bot}} C_{bottom}gdz + \int_{H_{bot}}^{H_{FR}} C_{freeboard}gdz + \frac{dP_{transition}}{dz} + \frac{dP_{riser}}{dz} \quad (30)$$

Secondly, the oxygen supply from oxygen carriers must fulfill the demand of the fuel based on Eq. (25), which is useful to obtain the mean reaction time. Thirdly, the circulation of the solids inventory can transfer some unburned carbon out of the fuel reactor, which has a significant impact on the conversion efficiency of the solid fuel. The amount of the unburned carbon out of the fuel reactor can be calculated as follows:

$$F_{carbon,out} = C_{carbon,coal}F_{coal,in}/M_C - [\left(F_{CO_2} + F_{CO} + F_{CH_4}\right)_{out} - F_{CO_2,in}] \quad (31)$$

The unburnt carbon would be entrained into the air reactor. As the

Table 3
Kinetic parameters of reduction reaction of oxygen carriers.

	CH_4	H_2	CO
k_0 ($mol^{1-n}m^{3n-2}s^{-1}$)	$8.0\cdot10^{-4}$	$2.3\cdot10^{-4}$	$6.2\cdot10^{-4}$
E (kJ/mol)	49	24	20
n	1.3	0.8	1.0
b	12	3	3

fluidization gas is air, the unburnt carbon can be oxidized to CO_2 completely, so the char conversion can be expressed as:

$$X_{Char} = (F_{coal}C_{fix} - Mw_c F_{carbon,out})/F_{coal}C_{fix} \quad (32)$$

Because fluid dynamics models for the transition zone and the riser are coupled with that of the fuel reactor, the variables at the outlet of fuel reactor are directly used as the initial values of the transition zone and the riser to solve the governing equations.

Fig. 3 presents how to carry out the simulation described above. The oxygen supply, the pressure drop and the char conversion shown in Eqs. (25), (30) and (32) are the main initial parameters. Before solving the equations, the average conversion of hematite particles can be obtained from Eqs. (23) to (24) by an iterative process. Then reduction rates of oxygen carriers are calculated. Once the whole calculation has converged, the new pressure drop, the oxygen supply and the char conversion can be obtained. These values would be compared to the initial value of them. If all values do not fit well, the new assumptions are made to another calculation process until the calculated values are equal to the initial values. It costs about 2 min to simulate each case in a personal laptop with 2G memory and one quad-core CPU.

4. Result and discussion

Five experimental cases are shown in Table.4 where case 3 is selected as the fundamental case to develop the model. Table 5 shows operation parameters for this fundamental case and the geometric information about the reactor. Then the measurements from other cases are used to validate the model. The effects of different operation conditions on the performance are analyzed in the following part.

4.1. Fluid dynamics and mass distribution

Fig. 4(a) shows the profiles of the gas velocity and the solids flow along the reactor height. The gas velocity increases gradually because of gas generation from the heterogeneous reactions in the bottom zone. Drying and pyrolysis happen instantaneously at height 0.1 m where the gas velocity has a sudden increase. The solids flux starts at the top of the bottom bed where the splash phase and core-annular flow begin. As seen in Fig. 4(b), the splash phase dominates the solids concentration that decreases obviously above the bottom zone. Fig. 4(c) shows that the molar flux of CO increases quickly at the bottom of the freeboard as char gasification continues to occur. However, the net productions of CO and H_2 are negative at the upper part of the upper zone, since the reduction rates of oxygen carriers are larger than the generation rate from char gasification. The concentrations of CO_2 and H_2O always increase along the reactor because they are mainly produced by the reduction of hematite particles.

The superficial velocity decreases at the upper of freeboard zone ($z > 0.6$ m), as shown in Fig. 4(a). This indicates the influence of the core-annulus structure on the gas velocity. The section area of core decreases from the outlet of fuel reactor to the calculated height where the thickness of the annulus reaches its saturation value. Because the gas is assumed to only flow in the core, its velocity decreases from the calculated height to the outlet. Meanwhile, the up-flow of the solids decreases because of the lateral transportation of particles from core to the annulus. The gas velocity increases sharply through the transition zone because of the quick contraction of the section area. The gas velocity in the riser is almost four times higher than that in the fuel reactor, so the driving force arising from the riser is enough to recirculate the oxygen carriers. The gas velocity in this riser with shorter length is so high, resulting in the relatively short residence time of solids and the relativly short reaction time of heterogeneous reactions. There is little change of the gas flow and volume fraction of solids in the riser, although the heterogeneous reactions are considered in this model.

Figs. 5 and 6 show the profile of gas concentrations in the bottom zone. The drying and pyrolysis products enter into the bubble phase firstly as the coal is fed (see Fig. 5). Therefore, the concentrations of N_2 and CO_2 decrease obviously, as seen in Fig. 6. The char gasification and reduction of oxygen carriers only occur in the emulsion phase in the model. Both the concentrations of H_2 and CO shown in Fig. 5(b) increase above the coal inlet because of the pyrolysis, the heterogeneous reactions and the diffusion from the bubble phase. N_2 enters the fuel reactor from the loopseal at height $z = 0.135$ m, so the concentrations of other gas species decrease. Since the CO_2 is diluted, the production of CO becomes slowly. Moreover, the WGSR and the reduction of oxygen carriers continue to consume CO. Therefore, the concentration of CO is decreased obviously but more H_2 is produced resulted from the WGSR. The total concentrations of gas species are determined by the molar flow of each species in both the emulsion and bubble phases. As shown in Figs. 5 and 6, the curves are similar to the simulated results in the literature [15].

4.2. Comparison with the experimental data

The experimental measurements are used to validate the model developed in this work. Fig. 7 shows the predicted and measured outlet gas concentration of case 1–4. The model provides a fairly good representation of the experimental data. Compared to other cases, the higher volume flow of fluidization gas decreases the residence time of hematite particles, so the combustible gases cannot be converted sufficiently in case 2. The higher operation temperature of case 4 greatly improves the combustion process, so the concentration of CO_2 reaches up to 90%.

The reactor performances are evaluated based on these calculation results. The char conversion rate, the CO_2 capture efficiency and the combustion efficiency are the important performance parameters for this 5 kWth unit. The char conversion rate is expressed in Eq. (32).

The combustion efficiency is directly related to the oxygen demand of complete combustion for combustible gas species. The oxygen demand in the fuel reactor is defined as:

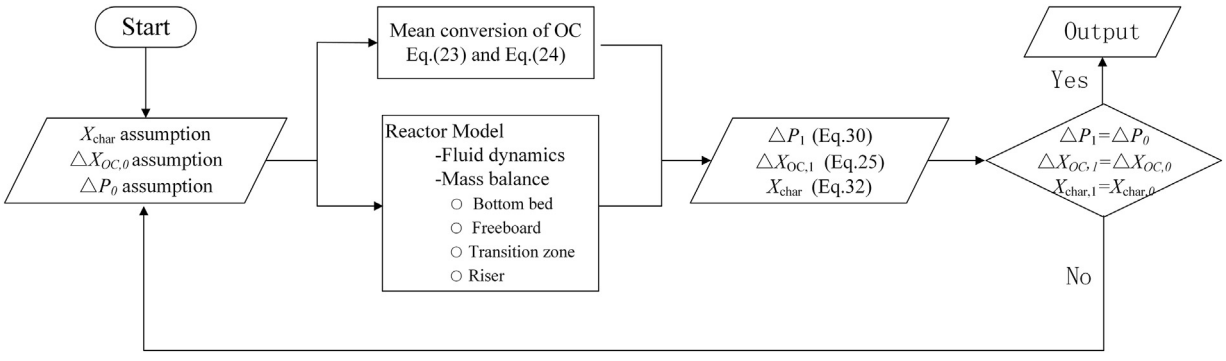

Fig. 3. Flowsheet of the model calculation.

Table 4
Operation conditions of five experimental cases.

Cases	P (kW)	Inventory (kg)	Temperature (°C)	Coal feed (kg/min)	Flux gas (L/min)	Volume ratio N_2:CO_2	△P (Pa)
1	2	2.5	950	4.1	25	20:5	5400
2	3.25	2.5	950	7.9	28	23:5	5500
3	4.75	2.5	950	11.3	25	20:5	5900
4	4.75	2.5	1000	11.3	24	20:5	4900
5	6	2.5	950	16	25	20:5	4770

Table 5
Operation parameters of standard case and reactor geometry.

Operating condition	value	Unit
Temperature T_r	950	°C
Pressure drop $\triangle P$	5900	Pa
Inlet gas flow F_{FR}	N_2:20, CO_2:5	L/min
Gas flow from loop seal F_{lp}	N_2:5	L/min
Coal feeding rate F_{coal}	11.3	g/min
Solid circulation rate F_{oc}	700	g/min
Initial bed inventory	2.5	kg
Reactor geometry		
Height of fuel reactor, H_{FR}	1000	mm
Diameter, D_{FR}	310	mm
Height of riser, H_{riser}	550	mm
Diameter, D_{riser}	45	mm
Height of coal feeding inlet	100	mm
Height of the return port from the loopseal	135	mm

$$\Omega_{OD} = (0.5Y_{CO} + 2Y_{CH_4} + 0.5Y_{H_2})/(\Phi_0(Y_{CO} + Y_{CH_4} + Y_{H_2})) \quad (33)$$

where the Y represents the volume fraction of gas compositions at the riser exit. Φ_O is the ratio of oxygen exhaustion to per mole of carbon for complete combustion. Therefore, the combustion efficiency can be calculated as:

$$\eta_{comb} = 1-\Omega_{OD} \quad (34)$$

The CO_2 capture efficiency is defined as the ratio of carbon emissions of the fuel reactor system to the total carbon emissions of this 5 KW_{th} unit. The unburnt carbon is entrained into the air reactor, and is oxidized to CO_2 directly. So the CO_2 capture efficiency is calculated by considering the unburnt carbon:

$$\eta_{cc} = (F_{CO_2,FR} + F_{CO,FR} + F_{CH_4,FR})/(F_{CO_2,AR} + F_{CO_2,FR} + F_{CO,FR} + F_{CH_4,FR}) \quad (35)$$

where $F_{CO_2,AR}$ is the flux of CO_2 produced from the full combustion of unburnt carbon in the air reactor.

Fig. 8 shows the predicted performance parameters of case 1, 2, 3 and 5 at the same temperature 950 °C with different thermal powers. It can be observed that relative errors of two performance parameters for different fuel power are within 10%. These results also validate the developed macroscopic model in this paper. The flow rate of N_2 as fluidization gas at 3.25 kW_{th} of fuel power goes up 15%, which decreases the combustion efficiency but increases the carbon capture efficiency. Thus, it is necessary to analyze how different operation conditions impact the performance parameters.

4.3. Operation temperature

The effects of operation temperature on the performance is shown in Fig. 9 where the fuel power is equal to 4.75 kW_{th}. It can be observed that the char conversion and the CO_2 capture efficiency increase more greatly as the temperature is less than 960 °C. The pressure drop of case 4 is 1000 Pa less than that of case 3 with the same coal feeding rate but different temperatures [34], which means more solids including oxygen carriers and char particles in case 4 are entrained out. Although higher temperature is good for the char gasification, less residence time of char

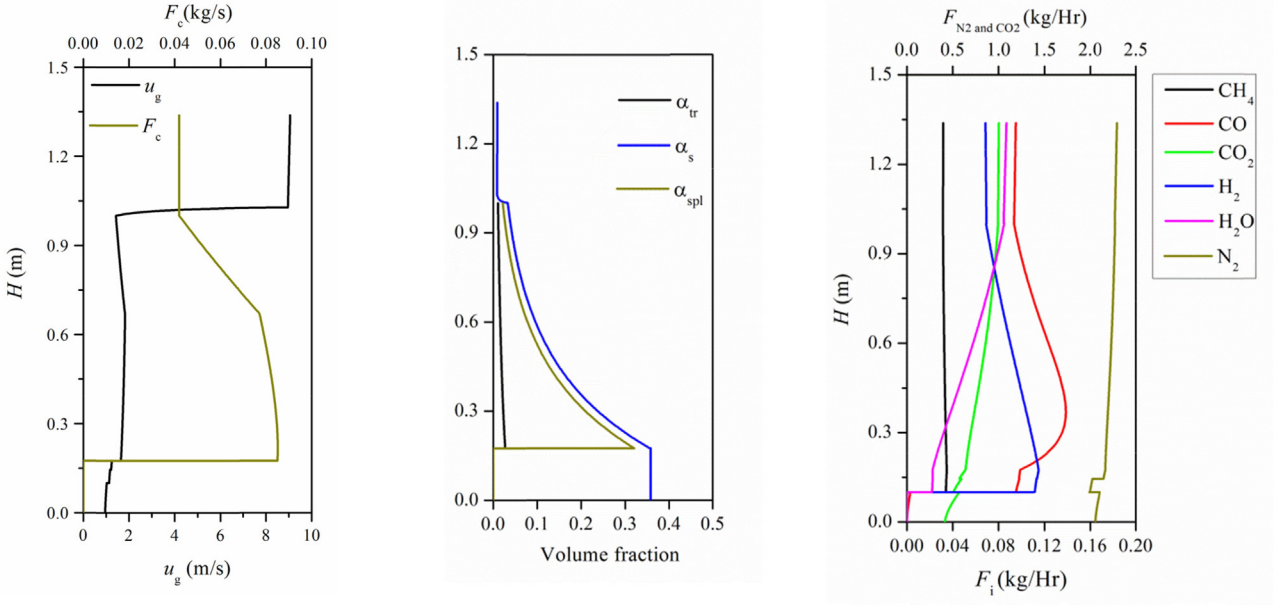

(a) Gas velocity and solid flux (b) Volume fraction of solid phase (c) Flux of gas compositions

Fig. 4. (a) Gas velocity and solid flux, (b) Volume fraction of solid phase, (c) Flux of gas compositions.

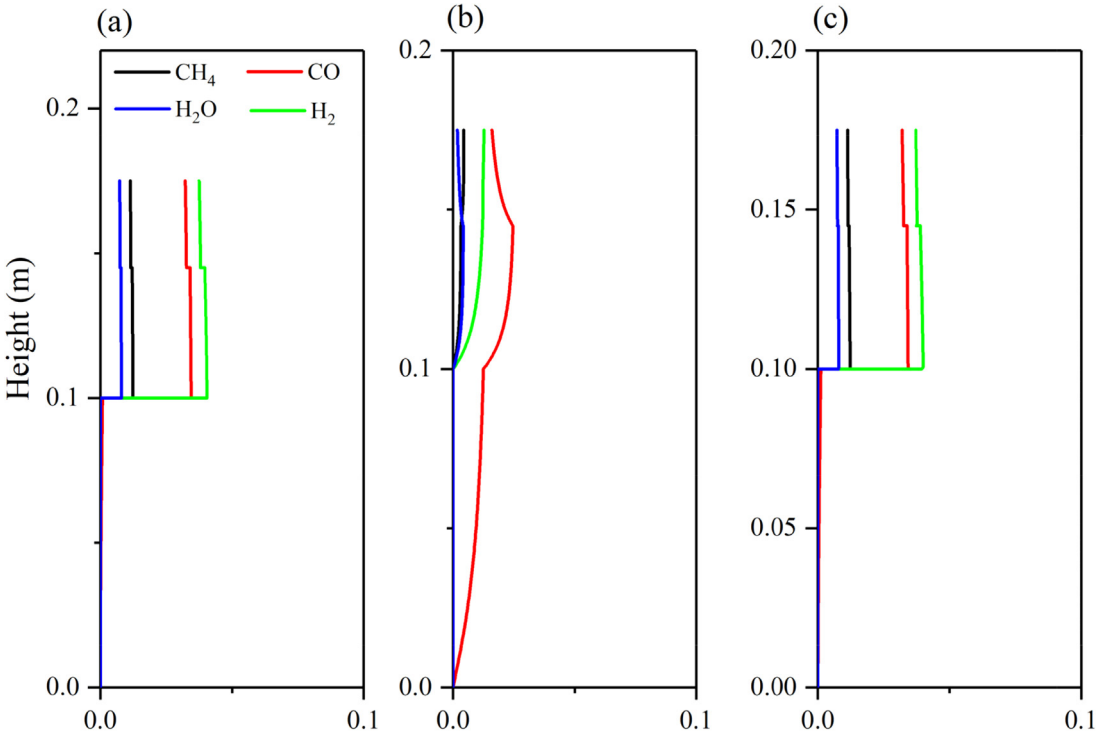

Fig. 5. Profiles of gas concentrations (CH_4, CO, H_2, and H_2O) in the bottom bed (a) gas in the bubble phase (b) gas in the emulsion phase (c) total gas in the bottom.

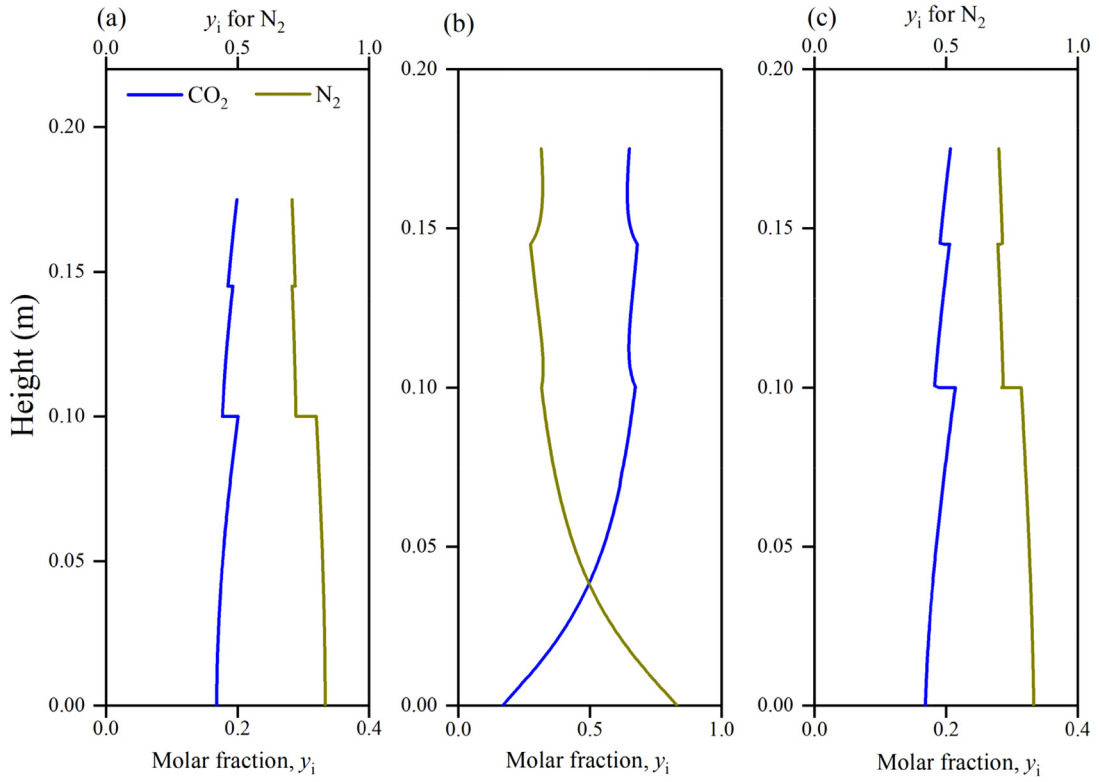

Fig. 6. Profiles of gas concentrations (CO_2 and N_2) in the bottom bed (a) gas in the bubble phase (b) gas in the emulsion phase (c) total gas in the bottom.

in the fuel reactor reduces this positive effect on the char conversion.

The combustion efficiency always increases with the increasing temperature but less dependent on the temperature than the char conversion and CO_2 capture efficiency. The higher temperature in the fuel reactor prompts not only the char gasification but also reduction reactions of hematite particles. Consequently, the reducible gases are almost oxidized by hematite particles at 1000 °C. As shown in Fig. 7, the molar fraction of CO_2 for case 4 is about 90%, so the oxygen demand decreases. The calculated combustion efficiency is about 91.2% that approximates to the measured value at temperature of 1000 °C. However, the higher temperature may result in the sintering phenomenon which will deteriorate the reaction performance of oxygen carrier

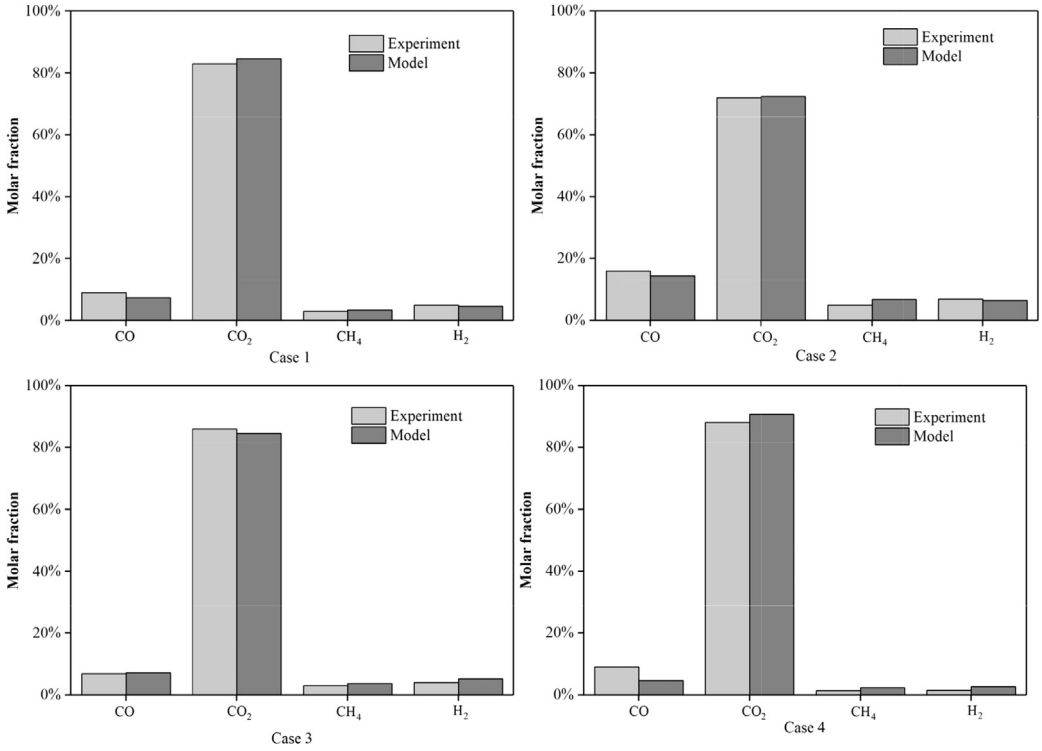

Fig. 7. Predictions of the gas concentration out of the fuel reactor against experimental measurements.

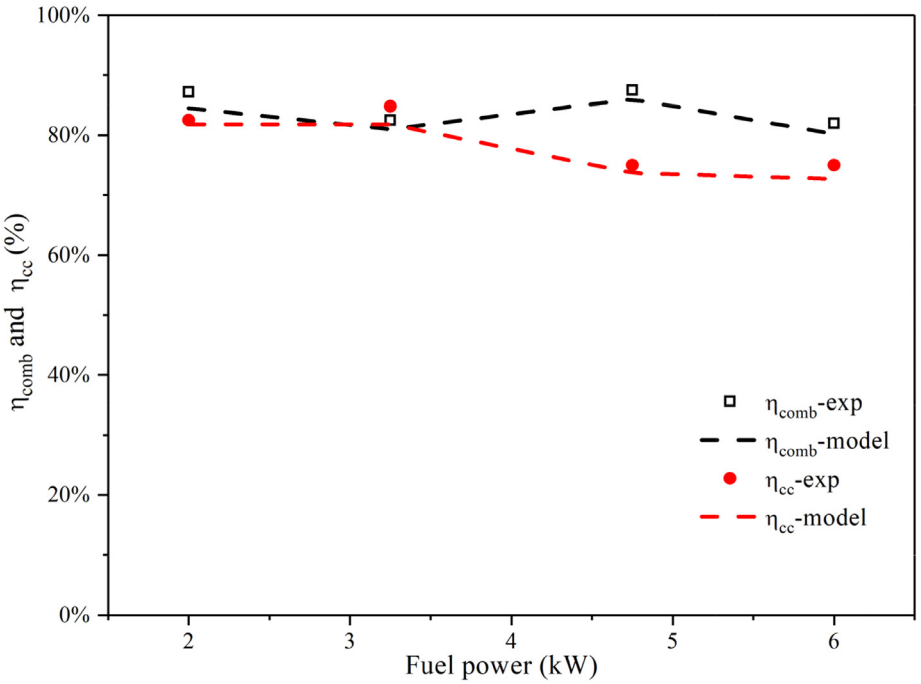

Fig. 8. Predicted combustion efficiency and carbon capture efficiency against the experimental measurements.

particles [43]. Usually the upper limit of operation temperature is set to 1000 °C.

4.4. Solid inventory in the fuel reactor

Fig. 10 shows the effect of the oxygen carrier inventory on the performance of different cases with the temperature 950 °C. The increase of the oxygen carrier inventory mainly leads to the increasing height of the bottom bed with the unchanged flux of the fluidization gas, which results in the longer residence times of solids [49]. For example, the calculated residence time of particles increases from 210 s to 910 s as the oxygen carrier inventory increases from 2.5 kg to 19 kg, which increases molar fraction of CO_2 at the outlet of the riser from 84.7% to 91.5%. At the moment, the combustible gases from gasification have enough time to be oxidized by the hematite particles. As a result, the combustion efficiency is also promoted with the increasing of solid inventory.

It can be noted the distinctive effect of the oxygen carrier inventory

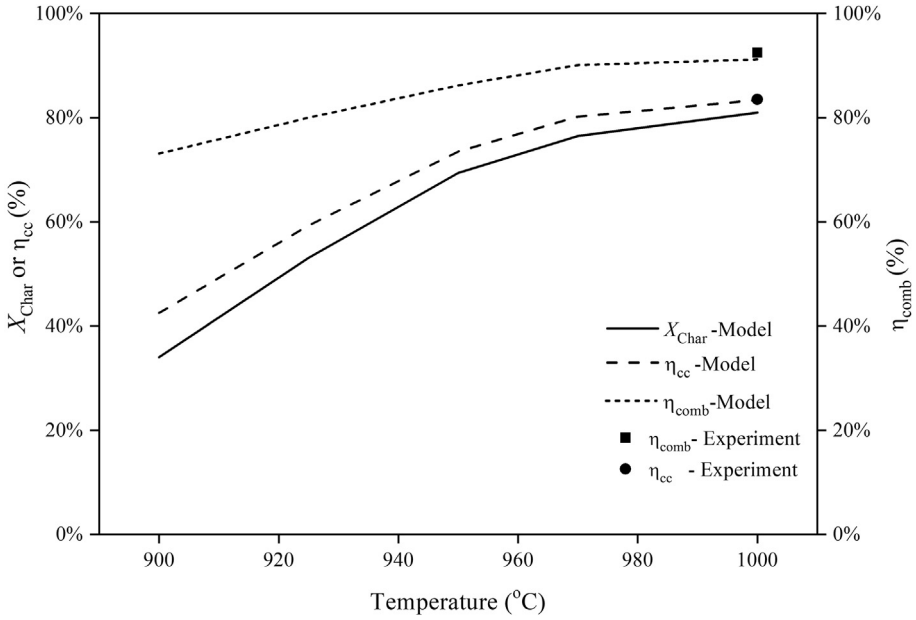

Fig. 9. Effect of the operation temperature in the fuel reactor on the performance parameters.

is relatively significant until the inventory is increased to 5.63 kg (corresponding the combustion efficiency about 89.7% and char conversion about 79%). The values of performance parameters change little when the solid inventory is higher than 5.63 kg. This predicted tendency has a good agreement with the measurements [50].

4.5. Oxygen carrier to fuel ratio

The oxygen carrier to fuel ratio plays a significant role in the combustion process. The oxygen supplied by hematite particles must fulfill the complete combustion of reducing gases. Fig. 11 shows the effect of oxygen carrier to fuel ratio on the combustion performance. The CO_2 capture efficiency, the char conversion rate and the variation of solids conversion decrease as this ratio increases. When the ratio is less than 1, the oxygen supply is insufficient for complete combustion, so the combustion efficiency has a sharp decrease trend with the decreasing of the ratio [31]. The simulated volume fraction of CO_2 increases from 84.7% to 87.4% for the ratio from 1.2 to 1.6, and reaches 88% when the ratio is 2. The volume fraction of reducible gases decreases slightly if the value of the ratio exceeds 1.6, namely, the combustion efficiency is continuously promoted with lower amplitude.

On the other hand, oxygen carrier to fuel ratio is proportional to the circulation flow of the bed inventory and expressed as $\phi = R_{O,hem}F_{OC}/\Omega_{coal}$ [31]. Increasing the ratio leads to the increase of the circulation flow under the condition that the solids inventory remains constant, which lowers the height of bottom zone and decreases the residence time of solids. This impairs the heterogeneous reactions and results in the decrease of the char conversion and the CO_2 capture

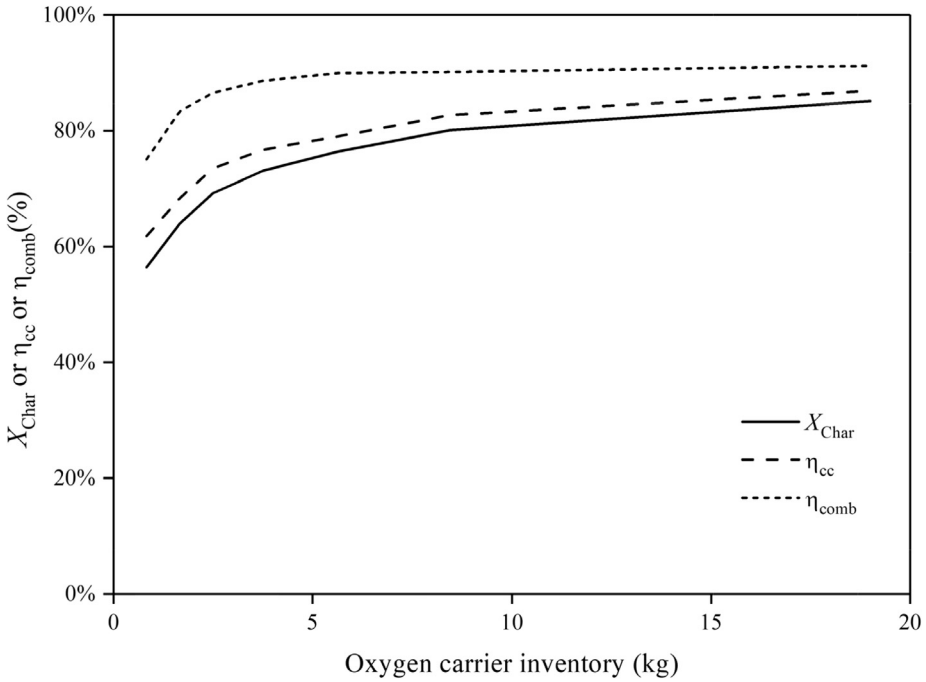

Fig. 10. Effect of solid inventory on the performance parameters.

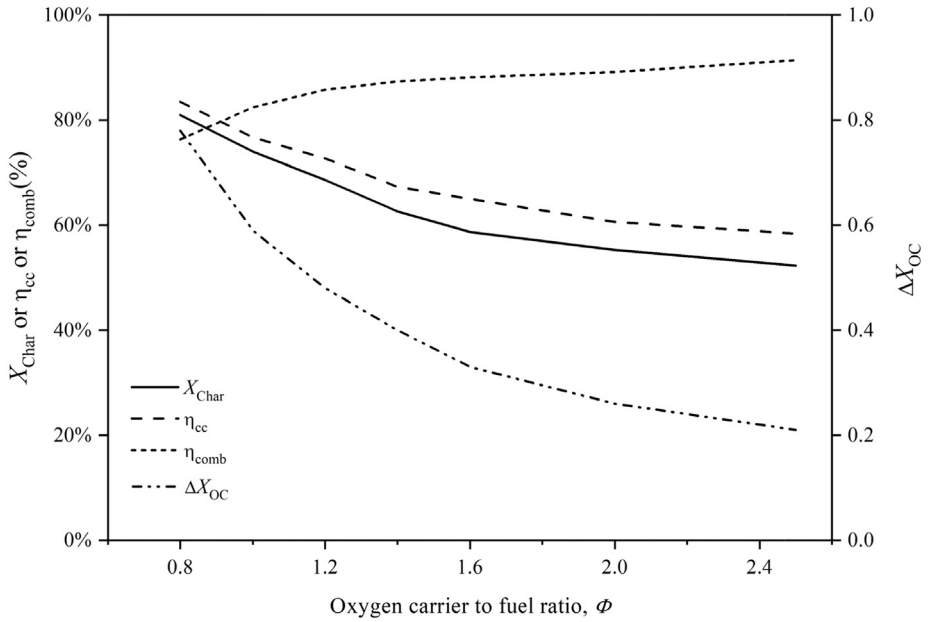

Fig. 11. Effect of the oxygen carrier to fuel ratio on the performance parameters.

efficiency. These predicted results are similar to the experimental evaluation in a continuous CLC reactor using coal as fuel [51]. Therefore, it is necessary to provide the sufficient residence time for the char gasification and the combustion of reducible gases in this experimental facility.

The variation of oxygen carrier conversion, $\Delta X = \overline{X_{OC,out}} - \overline{X_{OC,in}}$, can be used to evaluate the average reactivity of the oxygen carriers [52]. Fig. 11 shows that the decreasing speed of ΔX becomes lower gradually as the ratio exceeds 1.0, which means the plenty of oxygen carriers can provide oxygen continuously. Thus, it is important to keep the oxygen carrier to fuel ratio above 1.0 to maintain the higher average reactivity of hematite particles.

4.6. Mixture ratio of N_2 and CO_2

The effect of mixture ratio of N_2 and CO_2 as the fluidizing agent on the performance of the combustion process is evaluated. The motivation is that CO_2 can be supplied as the fluidization gas by recirculating a fraction of flue gas out of the fuel reactor. The total fluidization gas flow is 25 L/min. The tested N_2:CO_2 mixtures are set to 25:5, 20:10, 15:15, 10:20, 5:25 and 0:100. Fig. 12 shows that both the carbon conversion rate and the CO_2 capture efficiency increase for higher fraction of CO_2 because CO_2 can promote the char gasification [34]. The calculated total flow rate of CO and H_2 out of the fuel reactor increases from 0.088 mol/min to 0.264 mol/min. However, the increased flow rate of reducible gases has higher oxygen demand. However, the inventory of

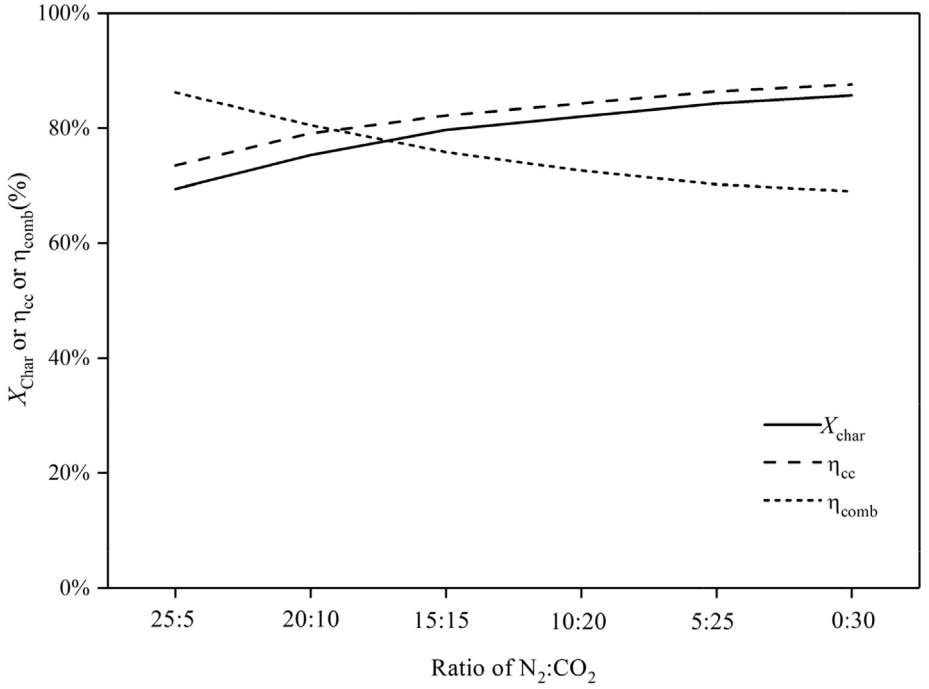

Fig. 12. Effect of mixing ratio of N_2:CO_2 as the fluidizing gas on the performance parameters.

hematite particles in these cases remains unchanged so that the active oxygen content supplied by the oxygen carriers keeps constant. Consequently, the combustion efficiency decreases with the increasing of CO_2 as fluidizing agent.

The mixing ratio of N_2 and CO_2 has less effect on performance improvement when the volume fraction of CO_2 reaches to 66.6%. This makes sense that the excessive gasification products in the fuel reactor lead to the increase of the superficial velocity. This brings about the difference of the solid circulation rate that decreases the residence time of particles. Thus the lower residence time of solids impairs the combustion process. The excessive amount of CO and H_2 as gasification products also inhibits the char gasification, which slows down the char conversion rate. These simulation results have similar trend to the experimental data [51].

4.7. Sensitivity analysis

Based on the results shown above, we conduct the sensitivity analysis to appraise how much different operation conditions influence the performance parameters. The relative linear sensitivity coefficients represents the sensitivity level and is defined as [24]:

$$\chi = \frac{\Delta v / v}{\Delta p / p} \tag{36}$$

where the v represents the target variable, p means the investigated parameters, Δv and Δp represent the change rate of the target variable and the investigated parameters, respectively.

The combustion efficiency and the CO_2 capture efficiency are chosen as the target variables, because the CO_2 capture efficiency has the similar trend to the char conversion rate. The target parameters are the four parameters discussed in previous section. Fig. 13 shows the value of relative linear sensitivity coefficient for each operation parameter. The positive value of χ means the positive effects of investigated parameters on the target variables.

It is obviously observed that the reactor temperature has the greatest contribution to the CO_2 capture efficiency and the combustion efficiency [53]. To determine the upper limit of temperature, the sintering behavior of hematite particles should be taken into consideration [43]. Compared to the solid inventory and the mixing ratio of N_2:CO_2 in the fluidization gas, the oxygen carrier to fuel ratio has higher relevance to the performance improvement in this experimental setup. The change of the oxygen carrier to fuel ratio can decrease the CO_2 capture efficiency but increase the combustion efficiency. Although the sensitivity coefficient for the solid inventory is low, it is worth noting that the increase on the solid inventory and the ratio of CO_2 in the fluidization gas is likely to offset the disadvantageous effect of the oxygen carrier to fuel ratio on the CO_2 capture efficiency.

5. Conclusion

The developed model is used to describe the fluid dynamics and mass transfer in the fuel reactor and riser of a new 5 kW_{th} interconnected fluidized bed reactor system. The model is validated by simulating different cases with various operation conditions. After that, how different operation parameters including the reactor temperature, the oxygen carrier inventory, the oxygen carrier to fuel ratio and the mixing ratio of N_2:CO_2 as fluidizing agent influence the char conversion rate, the CO_2 capture efficiency and the combustion efficiency are discussed, separately. Then the sensitivity analysis is also conducted to appraise the importance of four different operation parameters.

As the model can predict the flow of gas and solid phases, the conversion of fuel and oxygen carriers, and gas composition, etc., it provides an efficient tool to investigate the performance optimization for future reactor scaling-up and structure improvement. Some conclusions are obtained as follows:

(1) The reactor temperature has an important influence on the char conversion and CO_2 capture efficiency. Increasing the operation temperature will promote the char conversion and improve carbon capture efficiency obviously as the temperature is less than 960 °C.
(2) Increasing the bed inventory will extend the residence time of solids to improve the reactor performance, but too much inventory has no obvious contributon to combustion efficiency. The bed inventory loaded in the fuel reactor should be related to the coal feeding to obtain the best performance. Increasing the ratio of CO_2 as the fluidization gas also promotes the char conversion rate but decreases the combustion efficiency.
(3) The oxygen carrier to fuel ratio shows different effects on the performance, that is, to increase this ratio will be beneficial for a higher combustion efficiency however lead to a lower CO_2 capture

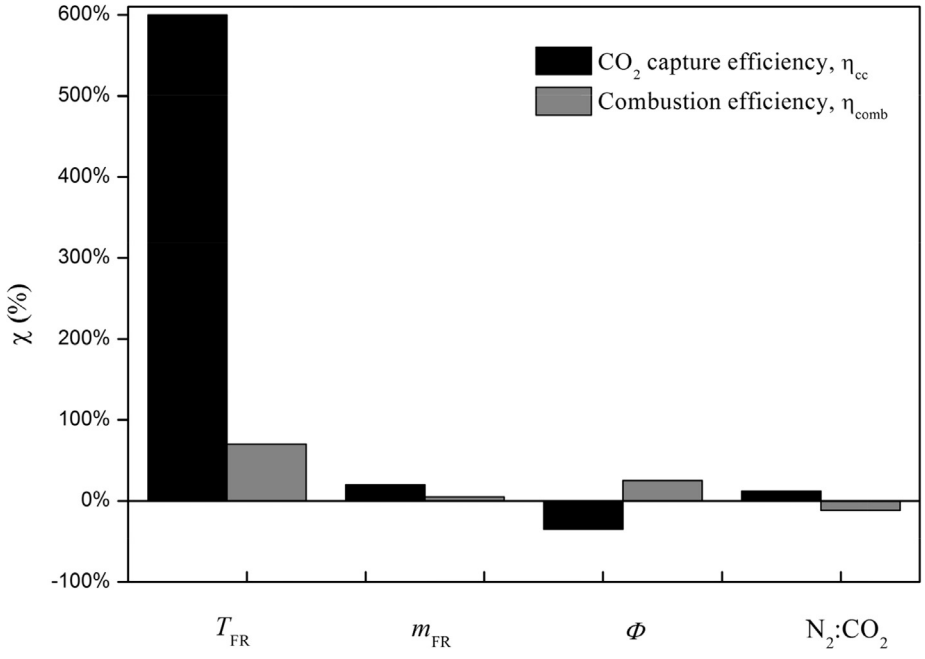

Fig. 13. Sensitivity analysis about the effect of different operation conditions on the performance parameters.

efficiency. Increasing the solid inventory and the content of CO_2 in the fluidization gas seem to be able to neutralize the negative effect of the ratio on the CO_2 capture efficiency and to improve the combustion efficiency for this experimental setup.

Acknowledgment

The authors were supported by “National Key R & D Program of China (2016YFB0600801)” and “National Natural Science Foundation of China (51522603)”.

Appendix A

See .

Table A1
Macroscopic model for Fuel reactor.

Bubble phase		Equation No.
if bottom is saturation		
Bubble fraction	$\delta_B = (\varepsilon_B - \varepsilon_{mf})/(1-\varepsilon_{mf})$	A1-1
Bubble velocity	$U_B = U_{B\infty}\delta_B/(1-\delta_B)$	A1-2
Interstitial gas velocity	$U_{g,int} = U_g - U_{vis} - U_{mf}(1-\delta_B)$	A1-3
Ratio of bubble flow to total flow	$\psi_{sat} = \frac{U_B}{U_g - U_{mf}(1-\delta_B)}$	A1-4
If bottom is not saturation		
Bubble velocity	$U_B = f_b(h + 4\sqrt{A_0})(U_g - U_{mf}(1-\delta_B))$	A1-5
Bubble fraction	$\delta_B = U_{vis}/(U_{vis} + U_{B\infty})$	A1-6
Single bubble velocity	$U_{B\infty} = 0.71\sqrt{gD_B}$	A1-7
Bubble size	$D_B = 0.54(U_g - U_{mf})^{0.4}(h + 4\sqrt{A_0})^{0.8}g^{-0.2}$	A1-8
Volume fraction of solids	$\varepsilon_B = (1-\delta_B)\varepsilon_{mf} + \delta_B$	A1-9
Saturation porosity	$\varepsilon_B = 0.5452 + \frac{495.5}{\Delta P0} + \frac{4.9\times10^{-6}}{d_p}$	A1-10
Bubble velocity	$U_B = f_b(h + 4\sqrt{A_0})(U_g - U_{mf}(1-\delta_B))$	
Throughflow velocity	$U_{g,int} = (1-f_b(h + 4\sqrt{A_0}))(U_g - U_{mf}(1-\delta_B))$	A1-11
Ratio of bubble flow to total flow	$f_b = (0.26 + 0.7e^{-3300d_p})/(0.15 + U_g - U_{mf})^{1/3}$	A1-12
Emulsion phase		
Minimum fluidization velocity	$U_{mf} = \mu_g(\sqrt{C_1^2 + C_2Ar} - C_1)/\rho_g d_p$, $C_1 = 27.2$ and $C_2 = 0.0408$	A1-13
Minimum fluidization porosity	$\varepsilon_{mf} = 0.586\phi^{-0.72}Ar^{-0.029}(\rho_g/\rho_s)^{0.021}$	A1-14
The governing equation for gas compositions		
For bubble phase		
$\frac{dF_{b,i}}{dV} = \delta_B k_{be}(C_{e,i} - C_{b,i}) + y_{e,i}\frac{dF_{exc}}{dV} - \frac{dF_{WGS,i}}{dV}$		A1-15
For emulsion phase		
$\frac{dF_{e,i}}{dV} = -(1-\delta_B)[\sum(-R_{g,i})_{OC} + \sum(-R_{g,i})_{char}]_e - \delta_B k_{be}(C_{e,i} - C_{b,i}) - y_{e,i}\frac{dF_{exc}}{dV} - \frac{dF_{WGS,i}}{dV}$		A1-16
The coefficient of mass transfer [54]		
$k_{be} = 1.631U_g Sc^{0.37}$		A1-17
Freeboard		
The solid mass flux from the bottom zone	$F_{0,i} = 131.1\left[\frac{A_c u_g}{\varepsilon_b}\rho_g\left(\frac{Re_{s,i}}{Ar_i}\right)^{0.31}\right]$	A1-18
The solid concentration in the transport phase	$C_{tri,i,H_b} = \frac{F_{0,i}}{A_{c,H}(u_{g,H_b} - u_{t,i})}$	A1-19
The solid concentration in the splash phase	$C_{spl,H_b} = C_{b,H_b} - C_{tr,H_b}$	A1-20
The solid concentration in the freeboard	$C_{freeboard} = C_{spl} + C_{tr}$	A1-21
The upflow flux of solid in the core	$F_{C,i} = C_{tr,i}A_C(U_g - U_{t,i})$	A1-22
The backflow ratio of particles at the outlet	$k_{b,j} = \frac{(F_{w,j})Hr}{F_{s,i}} = \frac{(F_C)Hr - F_{s,i}}{F_{s,i}} = 0.2$	A1-23
The total flow of char and oxygen carrier from the fuel reactor	$F_s = F_{s,OC} + F_{s,char}$	A1-24
The lateral diffusion of particle from the core to annular	$F_{t,j\|i} = F_{C,j\|i} - F_{C,j\|i+1}$	A1-25
The downflow flux of solid in the annular	$F_{w,j\|i} = F_{w,j\|i+1} + F_{t,j\|i}$	A1-26
The solid concentration in the annular	$C_{w,j} = \frac{F_{w,j}}{A_w u_{t,j}}$	A1-27
The contact coefficient between gas and particles in the freeboard	$\zeta_{gs} = 1 - 0.75\left(\frac{C_{frb}}{C_b(h = H_b)}\right)$	A1-28
The thickness of annular flow	$\delta_w = 0.01076(H_r - h)$	A1-29
The saturation value of thickness	$\delta_{w,sta} = 0.06456D_{reactor}$	A1-30
The height of core-annular flow	$h_{sta} = H_r - 6D_{reactor}$	A1-31
The governing equation for gas compositions		
$\frac{dF_{dil,i}}{dV} = -[\zeta_{gs}\sum(-R_{g,i})_{OC} + \sum(-R_{g,i})_{char}]_{spl} - [\zeta_{gs}\sum(-R_{g,i})_{OC} + \sum(-R_{g,i})_{char}]_{tr} - \frac{dF_{WGS,i}}{dV}$		A1-32
Contact efficiency between gas and particles [55]		
$\zeta_{gs} = 1 - 0.75[C_{freeboard}(h)/C_{bottom}(h = H_{bot})]^{0.4}$		A1-33

References

[1] J. Adanez, A. Abad, F. Garcia-Labiano, P. Gayan, F. Luis, Progress in chemical-looping combustion and reforming technologies, Prog. Energy Combust. Sci. 38 (2012) 215–282.
[2] A. Nandy, C. Loha, S. Gu, P. Sarkar, M.K. Karmakar, P.K. Chatterjee, Present status and overview of chemical looping combustion technology, Renewable Sustainable Energy Rev. 59 (2016) 597–619.
[3] A. Lyngfelt, B. Leckner, T. Mattisson, A fluidized-bed combustion process with inherent CO 2 separation; application of chemical-looping combustion, Chem. Eng. Sci. 56 (2001) 3101–3113.
[4] A. Lyngfelt, H. Thunman, Construction and 100 h of operational experience of a 10-kW chemical-looping combustor, Carbon dioxide capture for storage in deep geologic formations-results from the CO2 capture project 1 (2005) 625–645.
[5] Y. Cao, W.-P. Pan, Investigation of chemical looping combustion by solid fuels. 1. Process analysis, Energy Fuels 20 (2006) 1836–1844.
[6] J. Ströhle, M. Orth, B. Epple, Design and operation of a 1MW th chemical looping plant, Appl. Energy 113 (2014) 1490–1495.
[7] A. Thon, M. Kramp, E.-U. Hartge, S. Heinrich, J. Werther, Operational experience with a system of coupled fluidized beds for chemical looping combustion of solid fuels using ilmenite as oxygen carrier, Appl. Energy 118 (2014) 309–317.
[8] L. Shen, J. Wu, Z. Gao, J. Xiao, Characterization of chemical looping combustion of coal in a 1kW th reactor with a nickel-based oxygen carrier, Combust. Flame 157 (2010) 934–942.
[9] A. Cuadrat, A. Abad, L.F. de Diego, F. Garcia-Labiano, P. Gayan, J. Adanez, Prompt considerations on the design of chemical-looping combustion of coal from experimental tests, Fuel 97 (2012) 219–232.
[10] A. Abad, R. Perez-Vega, L.F. de Diego, F. Garcia-Labiano, P. Gayan, J. Adanez, Design and operation of a 50 kW(th) chemical looping combustion (CLC) unit for solid fuels, Appl Energ 157 (2015) 295–303.
[11] A. Lyngfelt, Chemical-looping combustion of solid fuels–status of development, Appl. Energy 113 (2014) 1869–1873.
[12] A. Lyngfelt, B. Leckner, A 1000MW th boiler for chemical-looping combustion of solid fuels–discussion of design and costs, Appl. Energy 157 (2015) 475–487.
[13] A. Bischi, Ø. Langørgen, I. Saanum, J. Bakken, M. Seljeskog, M. Bysveen, J.-X. Morin, O. Bolland, Design study of a 150 kWth double loop circulating fluidized bed reactor system for chemical looping combustion with focus on industrial applicability and pressurization, Int. J. Greenhouse Gas Control 5 (2011) 467–474.
[14] H. Ge, W. Guo, L. Shen, T. Song, J. Xiao, Biomass gasification using chemical looping in a 25 kWth reactor with natural hematite as oxygen carrier, Chem. Eng. J. 286 (2016) 174–183.
[15] A. Abad, P. Gayan, L.F. de Diego, F. Garcia-Labiano, J. Adanez, Fuel reactor modelling in chemical-looping combustion of coal: 1. model formulation, Chem. Eng. Sci. 87 (2013) 277–293.
[16] C. Linderholm, M. Schmitz, P. Knutsson, M. Källén, A. Lyngfelt, Use of low-volatile solid fuels in a 100 kW chemical-looping combustor, Energy Fuels 28 (2014) 5942–5952.
[17] N. Berguerand, A. Lyngfelt, Design and operation of a 10kW th chemical-looping combustor for solid fuels–Testing with South African coal, Fuel 87 (2008) 2713–2726.
[18] T. Song, J. Wu, H. Zhang, L. Shen, Characterization of an Australia hematite oxygen carrier in chemical looping combustion with coal, Int. J. Greenhouse Gas Control 11 (2012) 326–336.
[19] W. Shuai, L. Guodong, L. Huilin, C. Juhui, H. Yurong, W. Jiaxing, Fluid dynamic simulation in a chemical looping combustion with two interconnected fluidized beds, Fuel Process. Technol. 92 (2011) 385–393.
[20] H. Kruggel-Emden, S. Rickelt, F. Stepanek, A. Munjiza, Development and testing of an interconnected multiphase CFD-model for chemical looping combustion, Chem. Eng. Sci. 65 (2010) 4732–4745.
[21] M. Su, H. Zhao, J. Ma, Computational fluid dynamics simulation for chemical looping combustion of coal in a dual circulation fluidized bed, Energy Convers. Manage. 105 (2015) 1–12.
[22] P. Kolbitsch, T. Pröll, H. Hofbauer, Modeling of a 120kW chemical looping combustion reactor system using a Ni-based oxygen carrier, Chem. Eng. Sci. 64 (2009) 99–108.
[23] P. Peltola, J. Ritvanen, T. Tynjälä, T. Hyppänen, Model-based evaluation of a chemical looping combustion plant for energy generation at a pre-commercial scale of 100MW th, Energy Convers. Manage. 76 (2013) 323–331.
[24] P. Kaushal, T. Pröll, H. Hofbauer, Model for biomass char combustion in the riser of a dual fluidized bed gasification unit: Part 1—model development and sensitivity analysis, Fuel Process. Technol. 89 (2008) 651–659.
[25] K. Mahalatkar, J. Kuhlman, E.D. Huckaby, T. O'Brien, CFD simulation of a chemical-looping fuel reactor utilizing solid fuel, Chem. Eng. Sci. 66 (2011) 3617–3627.
[26] J.M. Parker, CFD model for the simulation of chemical looping combustion, Powder Technol. 265 (2014) 47–53.
[27] D. Pallares, F. Johnsson, Macroscopic modelling of fluid dynamics in large-scale circulating fluidized beds, Progr. Energy Combust. Sci. 32 (2006) 539–569.
[28] F. García-Labiano, L.F. de DIEGO, J. Adánez, A. Abad, P. Gayán, Reduction and oxidation kinetics of a copper-based oxygen carrier prepared by impregnation for chemical-looping combustion, Ind. Eng. Chem. Res. 43 (2004) 8168–8177.
[29] A. Abad, J. Adánez, F. García-Labiano, F. Luis, P. Gayán, Modeling of the chemical-looping combustion of methane using a Cu-based oxygen-carrier, Combust. Flame 157 (2010) 602–615.
[30] A. Abad, J. Adanez, L.F. de Diego, P. Gayan, F. Garcia-Labiano, A. Lyngfelt, Fuel reactor model validation: assessment of the key parameters affecting the chemical-looping combustion of coal, Int. J. Greenhouse Gas Control 19 (2013) 541–551.
[31] F. García-Labiano, F. Luis, P. Gayán, A. Abad, J. Adánez, Fuel reactor modelling in chemical-looping combustion of coal: 2—simulation and optimization, Chem. Eng. Sci. 87 (2013) 173–182.
[32] P. Peltola, J. Ritvanen, T. Tynjälä, T. Pröll, T. Hyppänen, One-dimensional modelling of chemical looping combustion in dual fluidized bed reactor system, Int. J. Greenhouse Gas Control 16 (2013) 72–82.
[33] P. Peltola, J. Ritvanen, T. Tynjälä, T. Hyppänen, Fuel reactor modelling in chemical looping with oxygen uncoupling process, Fuel 147 (2015) 184–194.
[34] J. Ma, H. Zhao, X. Tian, Y. Wei, S. Rajendran, Y. Zhang, S. Bhattacharya, C. Zheng, Chemical looping combustion of coal in a 5kW th interconnected fluidized bed reactor using hematite as oxygen carrier, Appl. Energy 157 (2015) 304–313.
[35] F. Johnsson, S. Andersson, B. Leckner, Expansion of a freely bubbling fluidized bed, Powder Technol. 68 (1991) 117–123.
[36] I. Aspen Technology, Aspen Custom Modeler. Version, Aspen Technology, Inc, Cambridge, Massachusetts, USA, 2006.
[37] H. Arastoopour, D. Gidaspow, Vertical countercurrent solids gas flow, Chem. Eng. Sci. 34 (1979) 1063–1066.
[38] G. Dzido, M. Palica, J. Raczek, Investigations of the acceleration region in the vertical pneumatic conveying, Powder Technol. 127 (2002) 99–106.
[39] W.C. Yang, A correlation for solid friction factor in vertical pneumatic conveying lines, AIChE J. 24 (1978) 548–552.
[40] M. Kumar, A.F. Ghoniem, Multiphysics simulations of entrained flow gasification. Part II: Constructing and validating the overall model, Energy Fuels 26 (2011) 464–479.
[41] G.-S. Liu, S. Niksa, Coal conversion submodels for design applications at elevated pressures. Part II. Char gasification, Prog. Energy Combust. Sci. 30 (2004) 679–717.
[42] R.C. Everson, H.W. Neomagus, H. Kasaini, D. Njapha, Reaction kinetics of pulverized coal-chars derived from inertinite-rich coal discards: gasification with carbon dioxide and steam, Fuel 85 (2006) 1076–1082.
[43] J. Adánez, L.F. de Diego, F. García-Labiano, P. Gayán, A. Abad, J. Palacios, Selection of oxygen carriers for chemical-looping combustion, Energy Fuels 18 (2004) 371–377.
[44] T. Song, T. Shen, L. Shen, J. Xiao, H. Gu, S. Zhang, Evaluation of hematite oxygen carrier in chemical-looping combustion of coal, Fuel 104 (2013) 244–252.
[45] A. Abad, J. Adanez, F. Garcia-Labiano, L.F. de Diego, P. Gayan, J. Celaya, Mapping of the range of operational conditions for Cu-, Fe-, and Ni-based oxygen carriers in chemical-looping combustion, Chem. Eng. Sci. 62 (2007) 533–549.
[46] G. Palchonok, A. Dolidovich, S. Andersson, B. Leckner, Calculation of true heat and mass transfer coefficients between particles and a fluidized bed, in: Proc of the 7th Engineering Foundation Conference on Fluidization, 1992, pp. 913–920.
[47] R. Chakraborty, J. Howard, Combustion of char in shallow fluidized bed combustors: influence of some design and operating parameters, J. Inst. Energy 54 (1981) 48–54.
[48] F. Bustamante, R. Enick, A. Cugini, R. Killmeyer, B. Howard, K. Rothenberger, M. Ciocco, B. Morreale, S. Chattopadhyay, S. Shi, High-temperature kinetics of the homogeneous reverse water–gas shift reaction, AIChE J. 50 (2004) 1028–1041.
[49] A. Cuadrat, A. Abad, P. Gayán, F. Luis, F. García-Labiano, J. Adánez, Theoretical approach on the CLC performance with solid fuels: optimizing the solids inventory, Fuel 97 (2012) 536–551.
[50] P. Markström, N. Berguerand, A. Lyngfelt, The application of a multistage-bed model for residence-time analysis in chemical-looping combustion of solid fuel, Chem. Eng. Sci. 65 (2010) 5055–5066.
[51] A. Cuadrat, A. Abad, F. Garcia-Labiano, P. Gayan, L.F. de Diego, J. Adanez, Effect of operating conditions in chemical-looping combustion of coal in a 500 W-th unit, Int. J. Greenhouse Gas Control 6 (2012) 153–163.
[52] J. Adánez, C. Dueso, L.F. de Diego, F. García-Labiano, P. Gayán, A. Abad, Methane combustion in a 500 Wth chemical-looping combustion system using an impregnated Ni-based oxygen carrier, Energy Fuels 23 (2008) 130–142.
[53] N. Berguerand, A. Lyngfelt, Chemical-looping combustion of petroleum coke using ilmenite in a 10 kWth unit− high-temperature operation, Energy Fuels 23 (2009) 5257–5268.
[54] M. Foka, J. Chaouki, C. Guy, D. Klvana, Gas phase hydrodynamics of a gas-solid turbulent fluidized bed reactor, Chem. Eng. Sci. 51 (1996) 713–723.
[55] S. Furusaki, T. Kikuchi, T. Miyauchi, Axial distribution of reactivity inside a fluid-bed contactor, AIChE J. 22 (1976) 354–361.